REVIEW ARTICLES

Physics of helicon discharges*

Francis F. Chen[†]

Electrical Engineering Department, University of California, Los Angeles, California 90095-1594

Because of their high density, low-pressure discharges ionized by helicon waves are being studied for their possible use in cluster tools for the fabrication of next-generation computer chips. How helicon waves are related to whistler waves and waves in a plasma-filled waveguide is explained, and the mystery of the high ionization efficiency is outlined. Experimental data on the waves and the equilibrium properties of the discharge are shown, and the status of our current understanding of the physical processes therein is summarized. The importance of kinetic effects and of a short-wavelength mode arising at low magnetic fields is evaluated. Applications of helicon discharges to such diverse fields as plasma accelerators, microwave generators, and tokamak physics are illustrated. Low-temperature plasma physics is often considered a discipline so different from high-temperature plasma physics that there is little overlap, but these studies show that the techniques developed in fusion and space plasma physics can be applied to technological plasmas as well. © *1996 American Institute of Physics.* [S1070-664X(96)92005-2]

I. INTRODUCTION

In experimental physics there are sometimes fortunate accidents in which the apparatus works so well that it takes years to understand why. Such was the case, for instance, with the CO_2 laser and the tokamak high confinement mode (H mode). Helicon discharges may be yet another example. Interest in helicon discharges stems from their unusually high ionization efficiency: plasma densities n achieved are almost an order of magnitude higher than in other discharges at comparable pressures and input powers. Helicon waves are basically low-frequency whistler waves (also called R waves) occurring in that region of the Clemmov–Mullaly–Allis (CMA) diagram where the frequency ω lies between the lower-hybrid frequency ω_{LH} and the electron cyclotron frequency ω_c, and well below the plasma frequency ω_p. In a cold, unbounded plasma, no other waves can propagate in this frequency regime. Harding and Thonemann[1] were the first to observe these waves in a bounded plasma, and it was Boswell[2] who showed that helicon waves could be used to generate gas discharges of high density. With only 1–2 kW of radio-frequency (rf) power, almost fully ionized plasma columns with $n \geq 10^{14}$ cm^{-3} can be produced.[2] Chen[3] has suggested that Landau damping of the waves could explain their rapid absorption, and, furthermore, that the phase velocities of these waves could generate primary electrons through the wave acceleration mechanism. Though there has been some evidence for fast electrons, these data are not incontrovertible; and the mystery of why helicon discharges are so efficient is still unresolved. Other possibilities are that the antenna coupling is especially effective and that the waves are absorbed anomalously via an instability.

It is well known that whistler waves in free space are right-hand (RH) circularly polarized; yet helicon waves in a cylinder can have either RH or left-hand (LH) polarization. To see how this comes about, consider the relative directions of the electric (E) and magnetic (B) fields in a plane electromagnetic wave in vacuum (Fig. 1). In both the RH and LH polarizations, the displacement current (J_d) is in such a direction as to regenerate the B field in the neighboring parts of the wave. In a low-frequency whistler wave (Fig. 2), J_d is negligible, the current being carried mainly by the $\mathbf{E} \times \mathbf{B}$ drift of the electrons. When the dc magnetic field $\mathbf{B}_0$ is in the same direction as the propagation vector $\mathbf{k}$, the RH wave has $\mathbf{J}$ in the same direction relative to $\mathbf{B}$ [Fig. 2(a)] as it did in the vacuum case [Fig. 1(a)], and so this polarization is possible. The LH wave [Fig. 2(b)], however, has $\mathbf{J}$ in the wrong direction to regenerate $\mathbf{B}$, and this polarization does not propagate. The same holds true if $\mathbf{B}_0$ is antiparallel to $\mathbf{k}$, as long as the polarization is defined relative to $\mathbf{B}_0$, and not to $\mathbf{k}$. Now if the wave is bounded, the wave amplitude must necessarily decrease toward the walls in order to satisfy the boundary conditions. This means that the current $\mathbf{J}$ must flow along $\mathbf{B}_0$ in order to maintain current continuity. However, finite inductance slows down the parallel flow and causes some charge pileup, which builds up a space-charge distribution. If the cylindrical container is long and thin, the accumulated charges appear across a small diameter, and a large electrostatic field is produced. This electrostatic field changes the nature of the electromagnetic whistler wave drastically and permits both RH and LH polarizations to occur.

The resulting electric field pattern is shown in Fig. 3 for the $m = +1$ (RH) and $m = -1$ (LH) modes. There is a critical radius r_c at which the E field changes sign because of the space charge there. Both polarizations are possible, though the LH mode is narrower than the RH mode. These patterns rotate in space without changing shape, so that a stationary

---
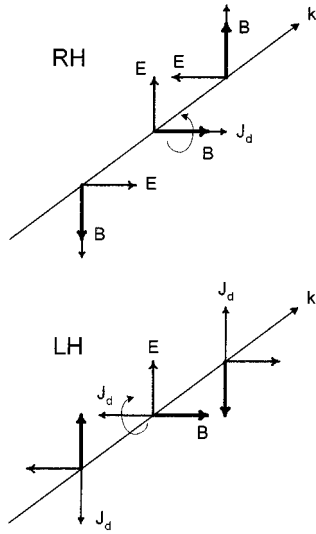
FIG. 1. Vector relations in right- and left-hand polarized electromagnetic waves in free space.
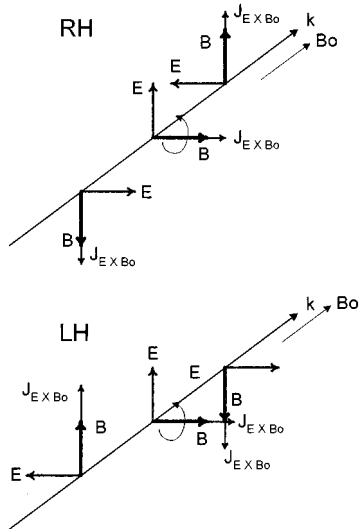

FIG. 2. Vector relations in right- and left-hand polarized low-frequency whistler waves in free space. The current in the LH wave is in the wrong direction for regenerating the B field.
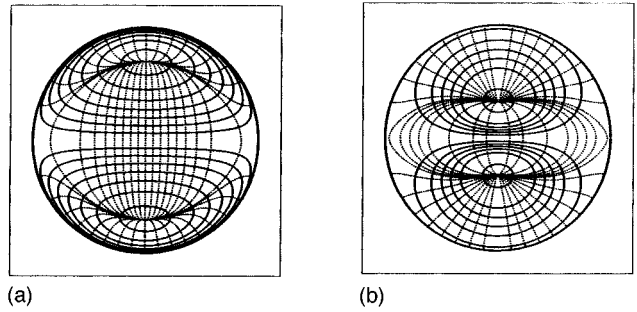

FIG. 3. Patterns of the electric (dotted) and magnetic (solid) field lines for the (a) $m=+1$ and (b) $m=-1$ azimuthal modes in a uniform plasma.

II. A SIMPLE MODEL OF HELICONS

The basic dispersion relation for helicon waves can be obtained easily in the limit of zero electron mass from the well-known equation for R and L waves in a cold plasma:

$$\frac{c^2k^2}{\omega^2}=1-\frac{\omega_p^2/\omega^2}{1\mp(\omega_c/\omega)\cos\ \theta}, \tag{1}$$

where θ is the angle of propagation relative to $\mathbf{B}_0$. For $\omega\ll\omega_c$, only the R wave (upper sign) propagates, and we have

$$\frac{c^2k^2}{\omega^2}=+\frac{\omega_p^2}{\omega\omega_c\ \cos\ \theta}. \tag{2}$$

Here k is the total k, and $k_z=k\cos\theta$; thus, Eq. (2) can be written

$$k_{\text{total}}=\frac{\omega}{k_z}\ \frac{\omega_p^2}{\omega_c c^2}. \tag{3}$$

To conform with helicon terminology, we now define $\beta=k_{\text{total}}$ and drop the subscript on k_z, obtaining

$$\beta=\frac{\omega}{k}\ \frac{\omega_p^2}{\omega_c c^2}=\frac{\omega}{k}\ \frac{n_0e\mu_0}{B_0}. \tag{4}$$

In cylindrical geometry, for waves varying as $\exp[i(m\theta+kz-\omega t)]$, the condition $k_{\text{total}}^2=k_\perp^2+k_z^2$ is replaced by

$$\beta^2=T^2+k^2, \tag{5}$$

where T is set by the boundary condition

$$m\beta J_m(Ta)=-kaJ_m'(Ta)\approx0 \quad (ka\ll1). \tag{6}$$

For $m=1$, the lowest Bessel root is $Ta=3.83$. Thus, for $T\gg k$, we have approximately

$$\frac{3.83}{a}=\frac{\omega}{k}\ \frac{n_0e\mu_0}{B_0}\propto\frac{\omega}{k}\ \frac{n_0}{B_0}. \tag{7}$$

This simple relation will suffice for discussion of experiments. Thus, for given n_0 and B_0, the dispersion relation $\omega(k)$ is a straight line, and for given ω and k, n/B is constant. For instance, if ω and B_0 are fixed and k is set by the antenna length, then when the density reaches the value given by Eq. (7), the conditions for helicon wave propagation will be met, and the rf absorption will be strong. In practice, the plasma has a nonuniform density distribution
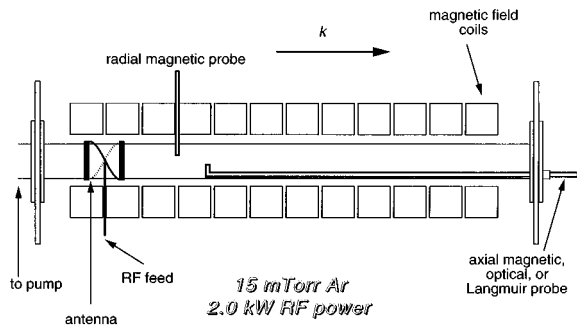
observer would see the $m=+1$ pattern rotating clockwise in time when viewed in the direction of $\mathbf{B}_0$. Note, however, that the local E field at a given radius can be RH polarized ($r<r_c$), LH polarized ($r>r_c$), or plane polarized ($r=a$). The nearly parallel bundle of E-field lines near the axis is primarily electrostatic in origin and is readily excited by the antenna, as described later.

FIG. 4. Schematic of the apparatus in which most of the measurements were made.

$n(r)$, and this has the effect of changing the resonant value of n/B. The helicon relation for arbitrary density profiles has been worked out,[4] and this modification has been used in comparing with the measurement shown below.

III. SOME EXPERIMENTAL RESULTS

To compare with theoretical predictions we show measurements made in a straight tube in a uniform magnetic field (Fig. 4). The tube is 2.5 cm in radius and 160 cm long, with an rf antenna at one end and ports for radial and axial probes. Typical operating conditions are 800 G, 2 kW of rf power at 27.12 MHz, and 15 mTorr of argon fill. Antennas used were of the Nagoya Type III variety, shown in Fig. 5. This type of
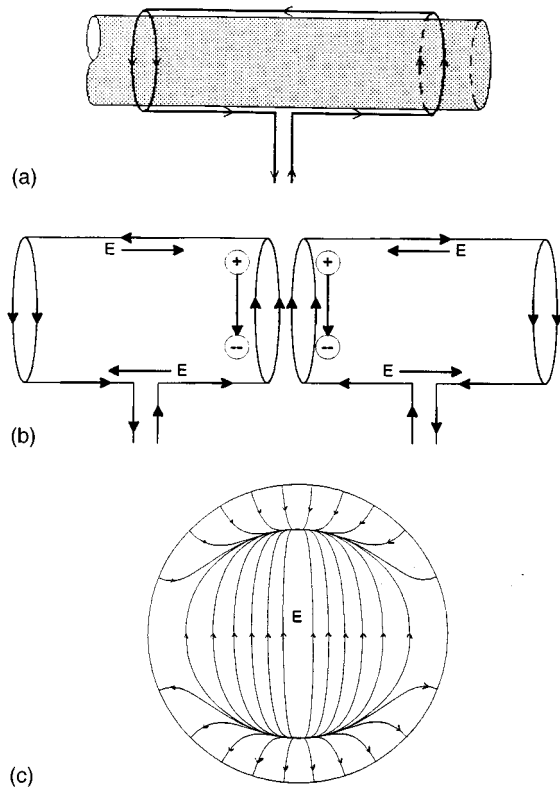

FIG. 5. (a) Schematic of a half-wavelength Nagoya Type III antenna. (b) Schematic of a full wavelength section of an infinitely long antenna, illustrating how electrostatic charges are created inside the plasma by the induced parallel electric field. (c) The E-field pattern of an $m=1$ mode.
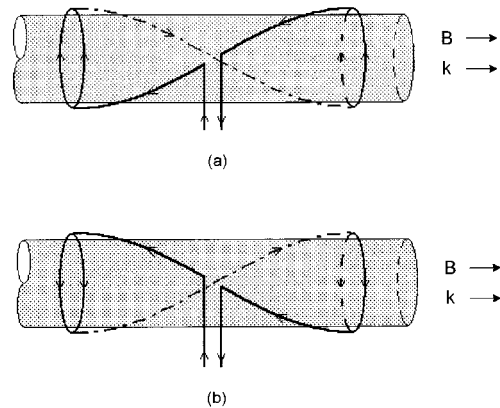

FIG. 6. (a) Right-helical and (b) left-helical antennas.

antenna converts an inductive field into an electrostatic field, as illustrated in Fig. 5(b), where two adjacent half-wavelength antennas are shown. The legs of the antenna that lie parallel to $\mathbf{B}_0$ provide the main effect. As the current J in these legs rises, a field E_z in the opposite direction is induced. Space charge then builds up until the electrostatic E_z field from these charges cancels the induced E_z field, since the total E_z field in a highly conducting plasma has to be nearly zero. Because of the $m=1$ azimuthal symmetry, the space charge at the opposite side of the diameter is of opposite sign, and this gives rise to a transverse E field that goes through the center of the plasma, much like the E field at the center of the $m=1$ mode pattern [Fig. 5(c)]. This type of antenna is efficient because it converts an electromagnetic signal into an electrostatic one and can create a field pattern with considerable overlap with the electric field of the wave. To couple to circularly polarized waves, we use RH and LH helical antennas (Fig. 6) that match the field patterns of the $m=+1$ and -1 modes, respectively. With any of these antennas, agreement with the basic linear relationship between n_0 and B_0 is found above rf powers of about 400 W, confirming the existence of helicon waves.[5]

A. Wave structure

The B_r, B_θ, and B_z components of the wave magnetic field were measured[6] as a function of radius with magnetic probes. The results are shown in Fig. 7 with theoretical curves for the $m=+1$ and -1 modes, computed for the measured density profile. Good agreement with the $m=+1$ mode is obtained when using the RH antenna, as expected. In particular, the zero-crossing for B_θ is at the right position for an $m=+1$ mode and does not agree at all with that for an $m=-1$ mode. When the direction of $\mathbf{B}_0$ is reversed, the RH antenna should excite an $m=-1$ mode. However, Fig. 8 shows that in this case the measured fields agree better with the $m=+1$ mode than with the $m=-1$ mode. Indeed, the direction of rotation was verified with two probes at 90° to be clockwise. With the straight Nagoya III antenna, which should excite both modes equally, only the $m=+1$ mode was observed. This bias toward RH polarization and the difficulty in exciting the $m=-1$ mode are not yet understood.

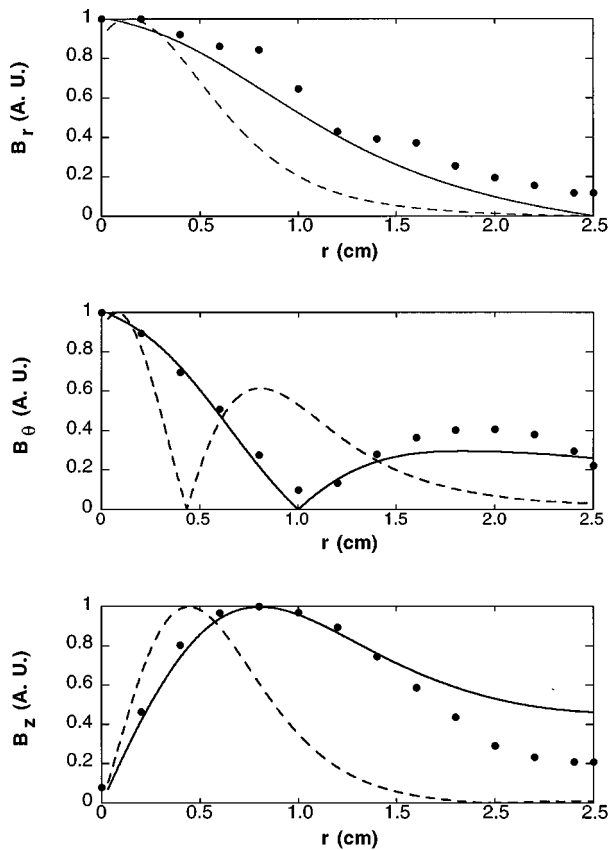The variation of B_z in the axial (z) direction was mea-

FIG. 7. Measured (points) and calculated (lines) components of the wave magnetic field in a 7.5 mTorr argon discharge at 800 G. A right-helical antenna was used. The solid curve is for the $m=+1$ mode; and dashed curve for the $m=-1$ mode. These curves were calculated for the measured density profile.

FIG. 8. Same as Fig. 7, but with the dc magnetic field reversed. In this case, the RH antenna is expected to launch an $m=-1$ mode.

sured with the long dogleg probe shown in Fig. 4, using a fixed probe as a reference. The variation of the local wavelength is shown in Fig. 9, together with the density measured with a Langmuir probe. It is seen that the wavelength varies inversely with the density, as predicted by Eq. (7). When the magnitude $|B_z|$ is plotted against z, however, a surprising result is found.[7] A large modulation of the wave amplitude appears (Fig. 10), suggesting the presence of standing waves. This cannot be a standing wave pattern, however, because the amplitude at the far end of the discharge is too small and, furthermore, the spacing between minima does not correspond to half the wavelength. The modulation is probably caused by the simultaneous excitation of two helicon modes by the antenna. From the k spectrum of the antenna currents, one finds that only two of all the possible helicon modes have k values that lie inside the largest peak of the antenna spectrum. These are the first two radial modes of the $m=+1$ azimuthal perturbation. The beat pattern computed with these two modes is also shown in Fig. 10, and it correctly predicts the positions of the first two minima.

B. Discharge equilibrium

A good deal about how the discharge is maintained and about the role of the helicon waves can be learned from
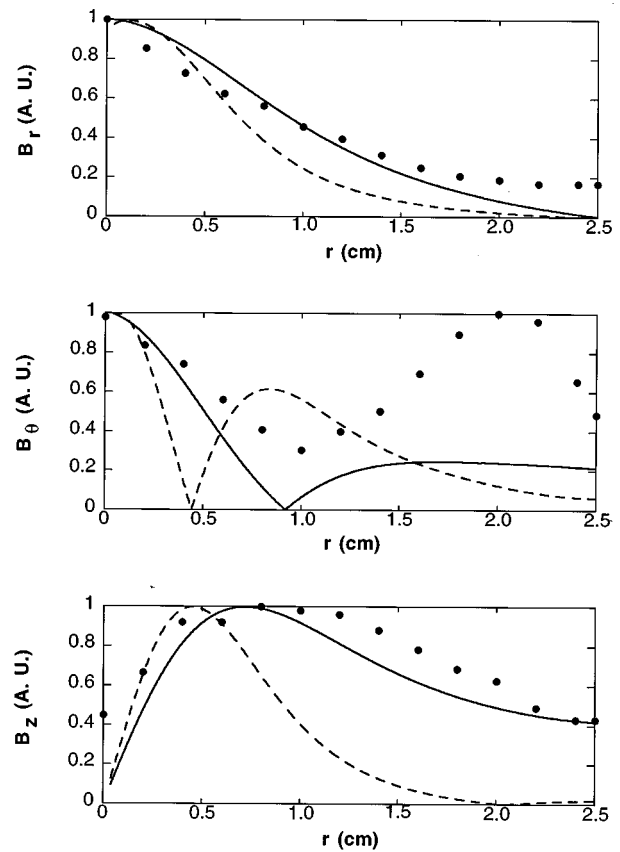
radial and axial profiles of density n, electron temperature T_e, and space potential V_s obtained with rf-compensated Langmuir probes.[8] Figure 11 shows that V_s is approximately constant along z, as one would expect in a highly conducting plasma. The axial profiles of T_e and n, however, show unexpected variations, in spite of the fact that the discharge col-
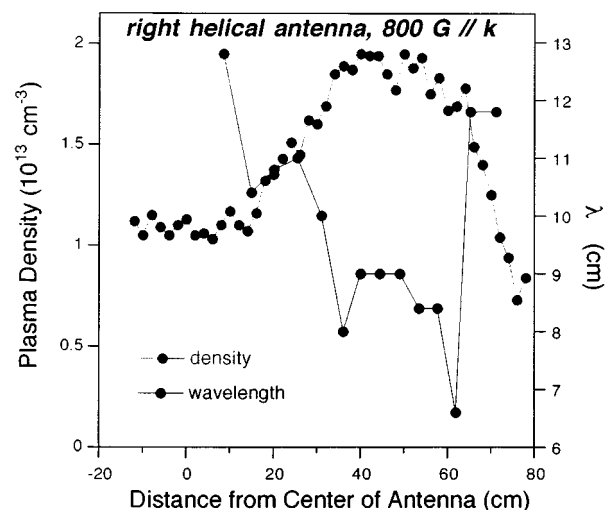

FIG. 9. Variation of local wavelength along the axis (lower curve), compared with the density variation (upper curve).
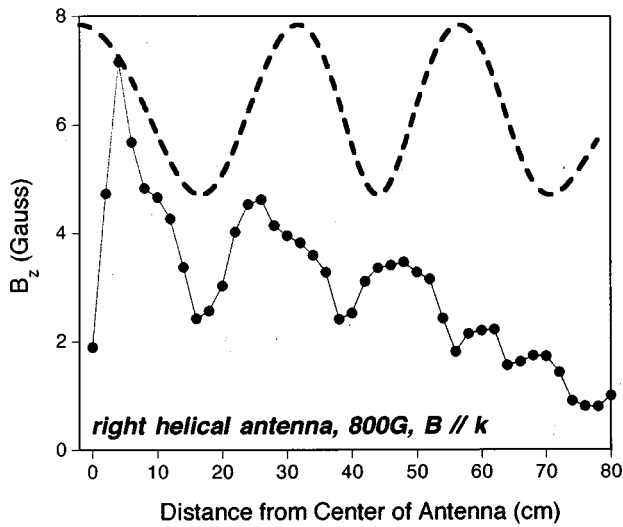
FIG. 10. Modulation of the amplitude $|B_z|$ along the axis, as measured (points) and computed (dashed line).

FIG. 12. Axial profiles of electron temperature and plasma density. The end rings of the antenna are indicated by the shaded bars.

umn appears visually to be quite uniform over the first meter of length. In Fig. 12 it is seen that T_e peaks within a wavelength of the antenna and then decays monotonically farther downstream. The density, however, rises downstream of the antenna and reaches a broad peak about 50 cm downstream before finally decaying as the plasma is lost to the walls. This behavior is contrary to intuition, since one would expect the ionization to be weak far downstream, where T_e is low; furthermore the cross-field diffusion losses are large there because of the large collision cross section at low temperatures. The possibility that there is a large downstream population of fast electrons accelerated by the wave can be rejected because the measured amplitude of the wave is too small to do this, and because no such electron tails appear in the probe curves. The downstream density peak can, however, be explained by the simple mechanism of pressure balance. Since the net force on the electrons parallel to B_0 must be nearly

zero, and since E_z was seen to be small, the electron pressure nKT_e must be nearly constant. The density rises in the downstream region simply because the temperature falls. To show this quantitatively, we have plotted the parallel electric and pressure-gradient forces on the electron fluid in Fig. 13. It is seen that these are approximately equal and opposite, except in the low-density region far from the antenna, where the rf compensation is inadequate, and the measured value of E_z may be in error.

Though the shape of the T_e curve in the region under the antenna and in its near-field is controlled by mechanisms that are not yet completely understood, the decay rate of T_e in the downstream region beyond the peak can be explained quantitatively. The data points of Fig. 12 for this region are reproduced in Fig. 14. If we assume that the electron thermal energy is transported downstream from the peak by classical
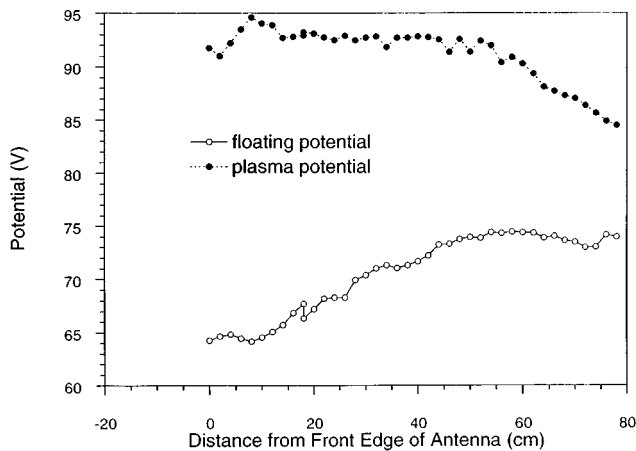

FIG. 11. Axial variation of space and floating potentials in a typical discharge. The space potential is measured directly from the inflection point in the probe characteristic, and it agrees with the values calculated from the floating potential and the local temperature.
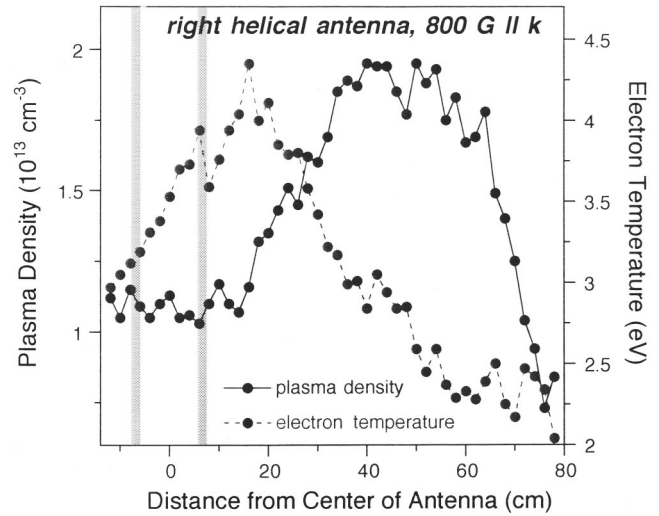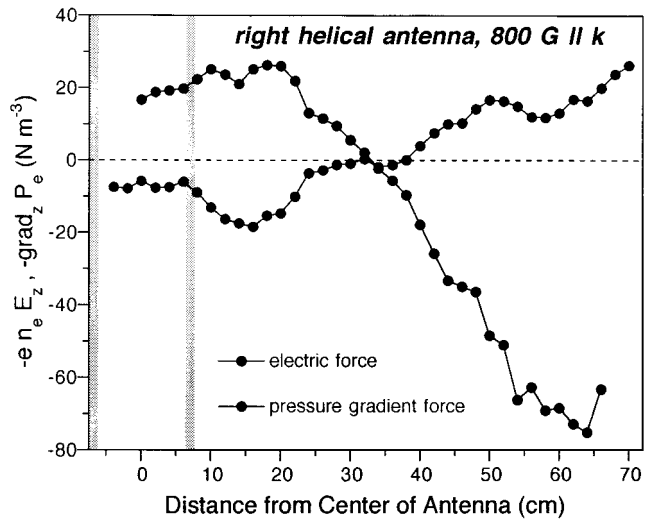

FIG. 13. Axial variations of the electrical force $-enE_z$ (the falling curve) and pressure gradient force $-\partial(nKT_e)\partial z$ (the rising curve) on the electron fluid along the magnetic field. These are calculated from the data of Figs. 11 and 12.
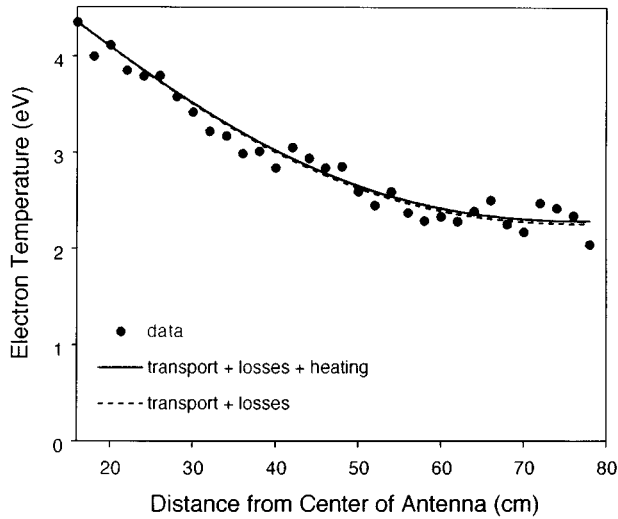
Francis F. Chen   1787

FIG. 14. The T_e data of Fig. 12, from the peak onward, as compared with calculations based on classical heat conductivity. The solid curve includes heat deposition by the measured helicon wave amplitude, while the dashed curve does not.
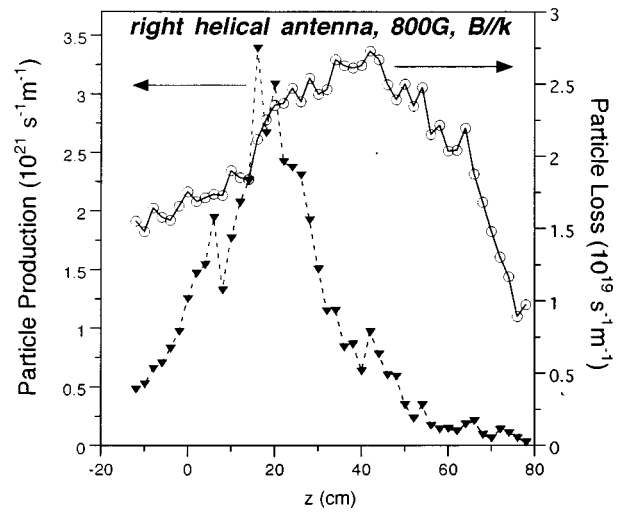

FIG. 15. Axial variation of ionization (triangles) and radial ambipolar diffusion losses (circles), as calculated from the data of Fig. 12 and corresponding radial profiles.

heat conduction, and that this energy is lost by inelastic collisions (mainly excitation of line radiation from ions), we can solve numerically for the temperature decay. The result is shown in Fig. 14 by the dashed line. We can also add the heating of the plasma by the damping of the helicon wave, using its measured amplitude, and that result is shown by the solid line. It is seen that the measured T_e variation is accurately reproduced, and that the contribution of the wave is negligible in this region. From the slope of the T_e curve, one can calculate the heat flow crossing the plane where T_e peaks. This turns out to be 1.4 kW, or 70% of the 2 kW of rf energy applied to the discharge. Apparently, almost all of the energy is absorbed by the plasma in the short region near the antenna, and most of this flows in the downstream direction, where the wave is too weak to affect the electron heat content. The hypothesis of progressive acceleration of primary electrons by the helicon wave is not borne out by this picture. Nonetheless, as will be seen later, a helicon wave is essential to the production of high densities, even if its effect is concentrated in the near-field of the antenna.

Though almost no heat is added to the plasma in the downstream region, there is nonetheless appreciable ionization by the thermal electrons at 3–5 eV temperature. Having measured n and T_e at each position z, we can calculate the local ionization rate using standard cross sections. Once created, electron–ion pairs are lost mainly by ambipolar cross-field diffusion to the walls. The discharge tube is long enough that axial losses can be neglected. The ambipolar diffusion coefficient can be computed from the electron–ion and electron–neutral collision frequencies, each found using the measured local value of T_e. (In this case, electron–ion collisions can cause cross-field diffusion because the ions are not magnetized.) The results are shown in Fig. 15. It is seen that the ionization occurs mainly in the upstream region, where T_e is high, but the losses occur farther downstream, the expected result of magnetic confinement. However, the

total production and loss of plasma, integrated over the downstream region, disagree by almost two orders of magnitude, with the ionization being too high in spite of the fact that no ionization by wave-accelerated primaries has been included. This discrepancy can be resolved by incorporating the effect of ion pumping. The dense plasma column is an efficient ion pump: neutrals which normally would flow to the pump end of the chamber at room temperature are ionized and then accelerated by presheath electric fields so that they flow to the end of the tube at the ion-acoustic velocity, or a fraction thereof. We estimate that this effect lowers the neutral pressure by a factor of 4.8 from the static pressure measured in the absence of the discharge. Using this neutral depletion factor, we find that the integrated creation and loss rates of ion–electron pairs, calculated from measured quantities, agree with each other within 50%. The total power lost in radiation and particle losses also agrees with the rf input power to this order of magnitude.

C. Discharge initiation

Initial experiments on helicon discharges usually show discontinuous jumps in plasma density as the B field or the rf power is raised, indicating the onset of efficient ionization as various helicon resonances are struck. Such data depend on the setting of the matching network and are difficult to understand quantitatively. Recently, Degeling et al.[9] showed that at low rf power, the coupling to the plasma was capacitive ("E mode"), resulting in very low densities. At higher power inductive, but nonresonant, coupling ("H mode") occurs and the density rises more rapidly. At the highest powers, a helicon wave is generated ("W mode"), and the density rises steeply to very high values.

The onset of helicon wave ionization can be seen clearly in our axial profiles of 488 nm ionized argon light emission, taken with an optical fiber probe with a small lens at the tip. Figure 16 shows that at 0 G the light is weak and localized to the antenna region; this is a simple inductively coupled
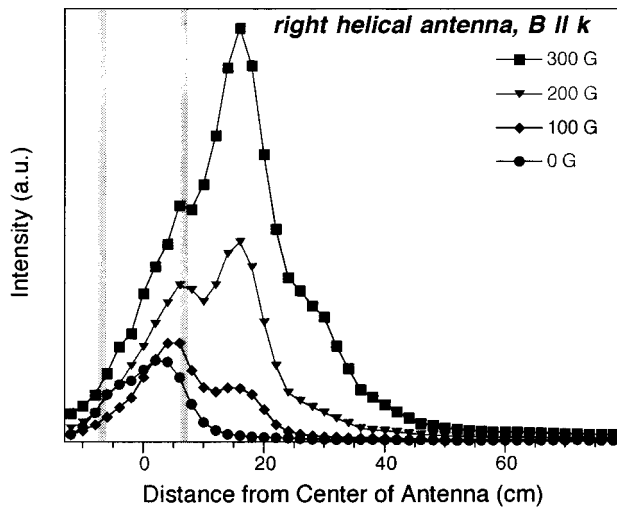
FIG. 16. Local optical emission measurements of the 488 nm Ar$^+$ line at various values of magnetic field.

plasma. At 100–200 G, a second peak appears about one wavelength downstream from the antenna. By 300 G, this helicon peak dominates. As the field is increased to 1000 G, the light emission continues to increase until it is >30 times that at 0 G. Further evidence that helicon wave generation is essential to the production of high densities is provided by Fig. 17, which shows the effect of reversing the magnetic field. The RH antenna then launches an $m=1$ mode backwards, in the direction of the pump. Although the excitation of the wave apparently takes place very near the antenna, the directionality of the effect leaves no doubt that this is not an ordinary inductively coupled discharge.

D. Kinetic effects

High-energy electrons with velocities in agreement with the phase velocity of the helicon wave have been reported by a number of groups. Our own measurements with Langmuir
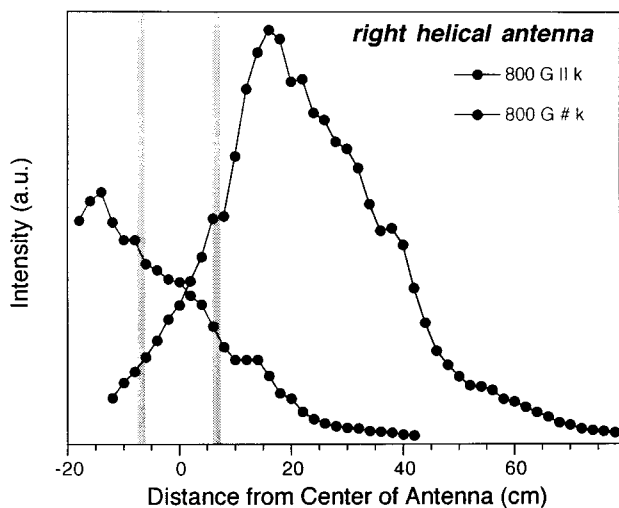

FIG. 17. Optical emission profiles with the magnetic field in the normal direction (higher curve) and in the reverse direction (lower curve).

probes, however, have always given pure Maxwellians, with no discernible sign of a high-energy tail. The results of such measurements depend on the type of rf compensation used and on the methods of interpreting the probe curves, such as the way in which ion current is subtracted. We have discovered a subtle effect which may explain the difference between our results and those of other groups. It arises from the pulsed nature of accelerated beams.

The method of rf compensation which we employ includes not only an rf filter but also a floating electrode which is close-coupled to the probe tip.[10] This forces the probe to follow fluctuations in floating potential V_f, which may be >100 V in amplitude. The dc averaged probe characteristic then reproduces the instantaneous characteristic accurately, and reliable measurements of T_e and V_s can be made. This would work even if there is a non-Maxwellian component, as long as it is constant. In wave acceleration or Landau damping, however, the accelerated electrons are bunched around that phase of the wave at which the electric field has its maximum backward amplitude. When these electrons strike the probe, the probe characteristic is changed, and V_f is shifted negatively. If the probe characteristic is shifted by feedback from V_f, the fast electron component will not appear in the dc averaged characteristic, though the thermal part will give the right value of T_e. In view of the severe effects of rf on distribution function measurements, it is clear that the details of the experimental technique are important for interpreting the results.

In addition to Landau damping or wave acceleration, there are other areas in which kinetic effects could be important even in partially ionized gas discharges such as the helicon discharge. One is the finite Larmor radius effect. In low-field operation, as discussed in the following section, wave accelerated electrons, whose velocities isotropize rapidly at these low temperatures, can have Larmor diameters of the order of centimeters. In this case, both the waves and the discharge can be affected by their finite Larmor radii. Second, when the magnetic field is low enough to approach the cyclotron frequency, there is the possibility of cyclotron damping[11] in addition to Landau damping. Third, the absorption of the rf power in a distance of the order of the wavelength and much shorter than the damping length suggests that there may be a beam–plasma instability excited by the population of wave-accelerated electrons. Indeed, in an experiment in which such a population is simulated by the beam from an electron gun, preliminary observations show that large oscillations occur and the beam is rapidly thermalized in the space of a few centimeters.

IV. HELICONS AT LOW MAGNETIC FIELDS

We have previously reported[5] the existence of a density peak, distinct from the usual helicon peak but still of order 5×10^{12} cm^{-3}, when the magnetic field is lowered to the order of 15–40 G. Exploitation of this effect could lead to more economical plasma sources. Since the condition $\omega \ll \omega_c$ no longer holds under these conditions, the simple results of Sec. II have to be extended to include finite electron mass

Phys. Plasmas, Vol. 3, No. 5, May 1996

Francis F. Chen   1789

m_e. From Maxwell's equations with the cold-plasma dielectric tensor, one can derive the following equation for the wave magnetic field:

$$\delta \nabla \times \nabla \times \mathbf{B} - k \nabla \times \mathbf{B} + \delta k_s^2 \mathbf{B} = 0, \tag{8}$$

where

$$\delta \equiv \frac{\omega}{\omega_c}, \quad k_s \equiv \frac{\omega_p}{c} \quad (\text{``skin number''}). \tag{9}$$

When $m_e = 0$, the highest-order term vanishes, and we are left with

$$\nabla \times \mathbf{B} = (\delta k_s^2 / k) \mathbf{B}, \tag{10}$$

which leads to the solution of Eq. (4). The full equation (8) factors into

$$(\beta_1 - \nabla \times)(\beta_2 - \nabla \times) \mathbf{B} = 0, \tag{11}$$

where β_1 and β_2 are the roots of

$$\delta \beta_j^2 - k\beta + \delta k_s^2 = 0. \tag{12}$$

Then

$$\mathbf{B} = \mathbf{B}_1 + \mathbf{B}_2, \quad \nabla \times \mathbf{B}_1 = \beta_1 \mathbf{B}_1, \quad \nabla \times \mathbf{B}_2 = \beta_2 \mathbf{B}_2, \tag{13}$$

where

$$\beta_{1,2} = \frac{k}{2\delta} \left[1 \mp \left(1 - 4\delta^2 \frac{k_s^2}{k^2} \right) \right]. \tag{14}$$

Here β_1 is the usual helicon root

$$\beta_1 \approx \frac{\delta k_s^2}{k} = \frac{\omega}{k} \frac{\omega_p^2}{\omega_c c^2} = \frac{\omega}{k} \frac{n_0 e \mu_0}{B_0}, \tag{15}$$

while β_2 is essentially a Trivelpiece–Gould mode (without a quasistatic approximation):

$$\beta_2 \approx k/\delta = k\omega_c/\omega \approx k_{\text{total}}, \tag{16}$$

or

$$\omega = \omega_c(k_z/k_{\text{total}}) = \omega_c \cos \theta. \tag{17}$$

The parabolic relationship, Eq. (12), between k and β gives a single value of k for each β:

$$k = \frac{\delta}{\beta}(\beta^2 + k_s^2). \tag{18}$$

This yields a minimum value of k, while the condition

$$k^2 = \beta^2 - T^2 \leqslant \beta^2 \tag{19}$$

gives a maximum value:

$$k_{\min} = 2\delta k_s, \quad k_{\max} = \left(\frac{\delta}{1-\delta} \right)^{1/2} k_s. \tag{20}$$

The k-β relationship is shown in Fig. 18 for various values of $\mathbf{B}_0$. For large $\mathbf{B}_0$, the parabola has a deep minimum; and for k near $k_{\max}$ the two branches are well separated, with $\beta_2 \gg \beta_1$. The left half of the parabola is the helicon branch, and the right half the Trivelpiece–Gould branch, which has large values of β and T, and thus very short radial wavelengths. In space physics it is well known[12] that whistler waves change their character for $\omega > \omega_c/2$: the phase velocity
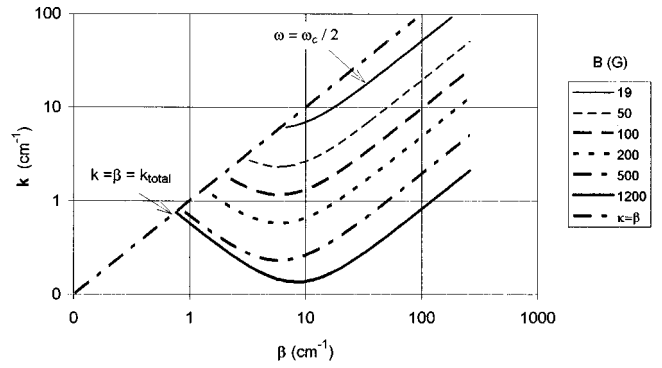

FIG. 18. Parabolic relation between parallel wave number k and total wave number β for various magnetic fields, with finite electron mass included. The curves are computed for $n = 2 \times 10^{13}$ cm^{-3}, $a = 2.5$ cm, $f = 27.12$ MHz, and $m = +1$.

decreases with frequency instead of increasing, and the group velocity loses its forward component, so that the wave is always a backward wave (with respect to $\mathbf{B}_0$). Figure 18 shows that helicon waves also have a critical frequency $\omega = \omega_c/2$: above this frequency the β_1 branch disappears, and only the β_2 branch is possible.

When the boundary conditions are taken into account, the two branches can be coupled. In the $m_e = 0$ limit discussed in Sec. II, the damping and electron inertia terms vanish, and the current j_z can flow without being driven by E_z, and we have $E_z = 0$. Thus the boundary condition for a conducting wall is simply $E_\theta = 0$. For an insulating wall, the boundary condition is $j_r = 0$, but j_r is proportional to B_r according to Eq. (10). Since B_r is proportional to E_θ by Faraday's law, the boundary condition is the same as for a conducting wall in this limit. When m_e is finite, however, electron inertia requires a nonzero value of E_z, even in the absence of collisions. Setting both E_θ and E_z to zero at the wall requires keeping both branches β_1 and β_2. This is for a uniform plasma in contact with a conducting cylinder. The situation changes in a complicated way if there is a vacuum or dielectric gap between the plasma and the wall,[13] if the conductor is far away, or if the plasma is nonuniform; but we cannot discuss these cases here. In general, a prescribed mixture of the two solutions $\mathbf{B}_1$ and $\mathbf{B}_2$ is required to satisfy the
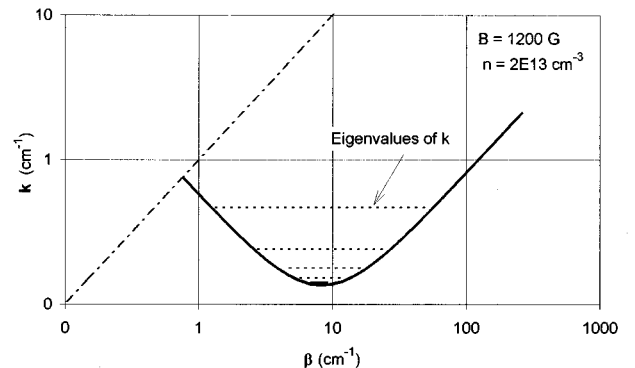

FIG. 19. Eigenvalues of axial wave number k at 1200 G, corresponding to various radial modes.

boundary conditions, and the permissible values of k are quantized. Figure 19 shows the eigenvalues of k for a typical high-field case. In this case, there are six possible values of k corresponding to different radial modes. The lowest radial mode, shown by the top line in Fig. 19, is almost a pure helicon mode, with a small admixture of the β_2 branch needed to satisfy $E_\theta = E_z = 0$. As expected, the mode pattern for this mode is not much different from that obtained with the $m_e = 0$ approximation. The fifth and sixth radial modes, lying near the bottom of the parabola, have almost equal parts of $\mathbf{B}_1$ and $\mathbf{B}_2$. As the field is lowered toward $\omega_c = 2\omega$, only one value of k near the bottom of the parabola is possible, and the wave contains large contributions from both branches. When damping is added, the amplitude of the β_2 (cyclotron) branch falls off rapidly away from the wall because of its short radial wavelength, and the interior solution is almost purely the helicon branch. The cyclotron branch then resembles a surface wave. These surface waves appear in computational treatments of antenna coupling to helicon waves, but they have not been seen in experiment. We believe that in practice the damping of the cyclotron branch is stronger than in theory, owing to such effects as finite electron Larmor radius, which are not included in the codes. The behavior of helicon waves at low values of ω_c/ω, and the proper theoretical treatment of them, have yet to be explored.

V. POSSIBLE APPLICATIONS

A. Semiconductor processing

The interest in helicon sources for etching and deposition of integrated circuits originally arose because of their high plasma densities and their versatility stemming from the numerous adjustable parameters, such as phase velocity and magnetic field strength and shape. Furthermore, the substrate bias is not tied to the rf power (and, thus, density) as it is in the standard capacitive discharge, so that the energy of ions striking the target can be controlled. The problem of particulate formation, which plagues plasma etchers operating at high pressures, is virtually eliminated in helicon reactors, which can operate in the 1 mTorr regime. Recently, interest has arisen in etching with both negative and positive ions, a process which minimizes device damage through charge trapping and which also increases the etch rate. Negative ions are produced in pulsed afterglows, in which electron temperature falls faster than density. We see from Fig. 12, however, that helicon discharges can give conditions of low T_e and high n simply by letting the plasma drift downstream, thus avoiding the problems of pulsing.

Many of the purported advantages of helicon discharges may never be realized in a practical sense, but at least one example of a commercially viable helicon source exists. This is the MØRI ($m = 0$ Reactive Ion) source manufactured by Plasma and Materials Technologies, Inc., shown in Fig. 20. This source uses an $m = 0$ antenna comprising two rings with opposing currents. (The $m = 0$ helicon mode is a more complicated animal which we could not treat here.) The matching network is distributed around the discharge tube. There are two independently adjustable magnetic coils lying in the same plane, and the plasma is trapped radially by a magnetic
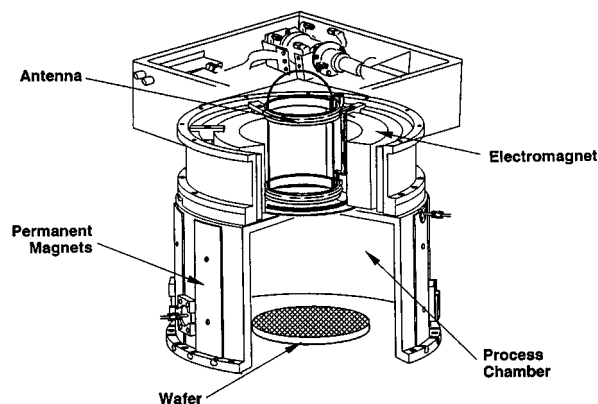

FIG. 20. A plasma source manufactured by PMT, Inc., based on the $m = 0$ helicon mode.

bucket formed by permanent magnets. This source has been demonstrated to give uniformity over a large area, high ion flux, and high selectivity and anisotropy. It has been used for etching silicon, dielectrics, and metals.

In future devices, one might cover even larger areas by using several helicon sources, or make a strip source suitable for web-coating continuous substrates. Neutral beam etching might be possible with a device such as the conceptual one shown in Fig. 21. Since there are large losses in converting ions to a collimated neutral beam, the helicon source is needed to provide the highest possible initial density.

B. Electrodeless beam sources

Regardless of whether or not helicon discharges can be shown to produce non-Maxwellian electron distributions, there is undocumented evidence that strong electron currents
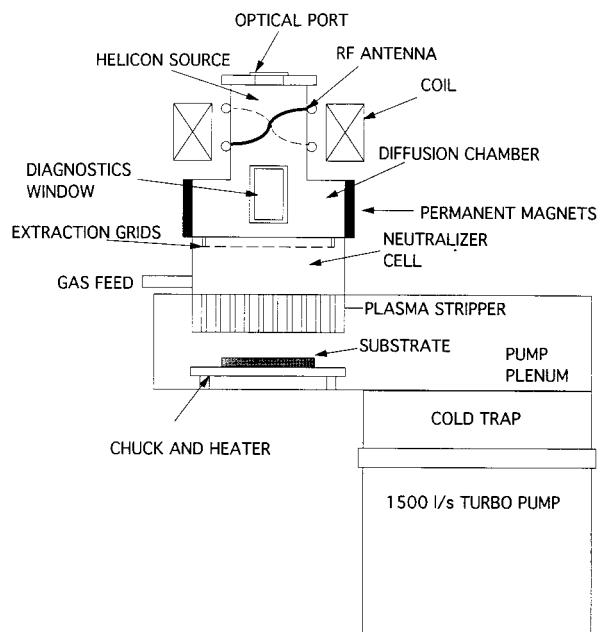

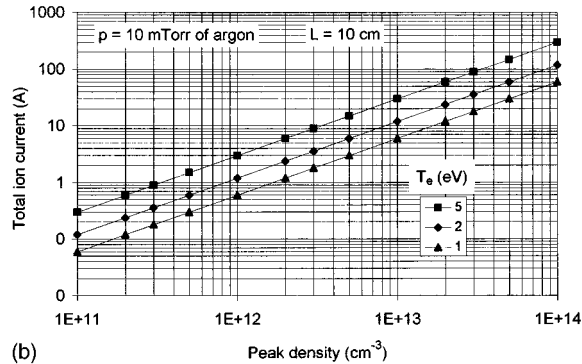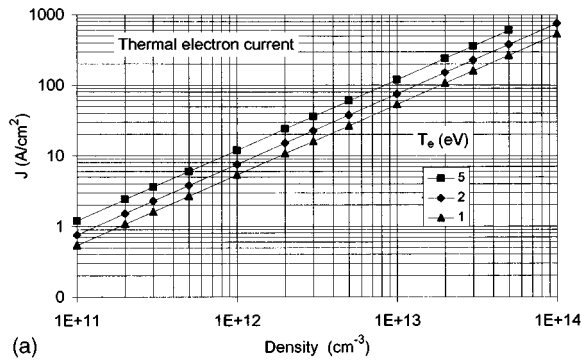FIG. 21. Conceptual neutral beam source for etching and deposition, based on an $m = +1$ helicon wave generator.

Phys. Plasmas, Vol. 3, No. 5, May 1996

Francis F. Chen   1791

FIG. 22. Thermal electron current along $\mathbf{B}_0$ versus plasma density for various values of KT_e.

FIG. 23. Two conceptual designs for a cathodeless electron beam source based on acceleration by helicon waves.

can be generated. It is rumored that solid endplates have been melted through by a steady-state helicon source. In early experiments,[14] we showed that a floating endplate is charged negatively to potentials greater than 200 V. Grounded endplates intercept electron currents of the order of 1 A. This current is limited by the ion current that can leave the discharge, since quasineutrality must be maintained. To extract a high-current electron beam from the source, an efficient mechanism for ion extraction must also be provided. Figure 22(a) shows the thermal electron current density leaving the end of a helicon discharge as a function of plasma density. As is well known, currents of order 100 A/cm^2 can be drawn at an average density of 10^{13} cm^{-3}. However, the ion current leaving the discharge across the magnetic field over a 10 cm length is about five times smaller at a pressure of 10 mTorr. This is independent of radius, since the surface area and the density scale length both scale as radius. To realize the beam-generating capabilities of the discharge, one has to increase the ion flux by either increasing the length over which the ions can leave or inducing ion loss, for instance, by ion cyclotron heating. Two possible configurations for beam sources are shown in Fig. 23. Such sources could be developed for microwave generators in communications satellites and would not depend on the reliability of oxide cathodes.

C. Laser accelerators

The beat-wave accelerator relies on a resonance between the plasma frequency and the beat frequency between two laser beam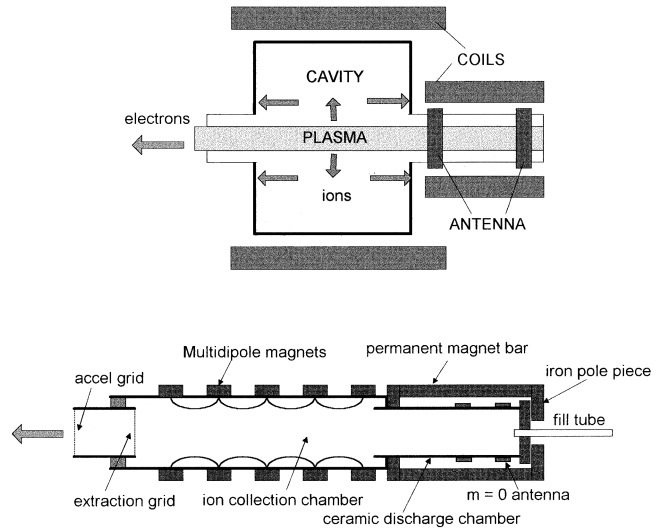s. The plasma density, therefore, has to be uniform to better than 1% over the acceleration length. Since the plasma frequency changes with the relativistic mass increase, acceleration could be done in stages, with a different plasma density in each. A conceptual schematic of such a staged accelerator was previously published,[15] but a helicon source could never provide the densities of order 10^{17} cm^{-3} required. A wake-field accelerator, however, excites the plasma waves on which the electrons surf by means of a lower energy electron beam or a short-pulsed laser beam. In this case, the plasma density can be of order 10^{15}–10^{16} cm^{-3} if the total length of the plasma is large enough. Figure 24 gives a conceptual sketch of an acceleration stage. Here two antennas would launch $m=-1$ helicon waves (if this can be achieved), and the magnetic field would be cusped, which has been found to give higher central densities.[16] A large plenum would allow a large amount of gas to be sucked into the discharge in each pulse. There would be differential pumping between the plasma chambers and the sections where the beam optics are corrected by quadrupole magnets. This kind of system can also give high enough densities for bringing high-energy beams to a final focus with an underdense plasma lens.
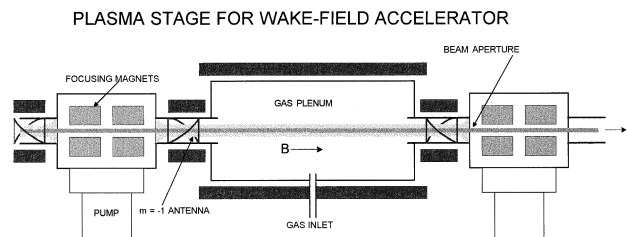

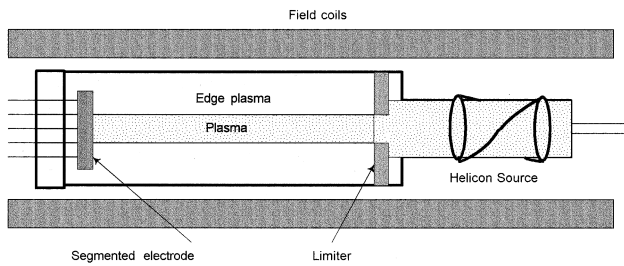FIG. 24. Conceptual layout of one stage of a wake-field accelerator.

FIG. 25. Possible use of a helicon source to generate a high-density, quiescent plasma for study of the effects of electric field shear.

D. Tokamak physics experiments

The use of helicon wave injection to fill a torus has already been done successfully by Loewenhardt et al.[17] in a heliac. To study stability of the tokamak H-mode E layer, Tynan et al.[18] have used a linear plasma generated by a reflex arc source. Such arcs are subject to the $\mathbf{E} \times \mathbf{B}$ instability and typically exhibit fluctuations of order 50%–100%. Replacing the arc with a helicon source, which is much more stable, would permit more careful studies to be done at fusion densities of order 5×10^{13} cm^{-3}. Such a device is sketched in Fig. 25.

Since helicon discharges can produce large electron currents, one might think of using helicon waves for tokamak current drive. However, if light ions are used instead of argon, the frequencies used for helicon discharges overlaps with those used for lower-hybrid or fast-wave current drive, and this research enters well-trodden territory. Nonetheless, the antennas used may be of some novelty if applied to auxiliary current drive used to tailor the current profile in reversed-shear discharges. After all, the Nagoya Type III antenna was originally invented in a fusion experiment![19]

ACKNOWLEDGMENTS

[1] G. N. Harding and P. C. Thonemann, Proc. Phys. Soc. **85**, 317 (1965).

[2] R. W. Boswell, Plasma Phys. Controlled Fusion **26**, 1147 (1984).

[3] F. F. Chen, Plasma Phys. Controlled Fusion **33**, 339 (1991).

[4] F. F. Chen, M. J. Hsieh, and M. Light, Plasma Sources Sci. Technol. **3**, 49 (1994).

[5] F. F. Chen and G. Chevalier, J. Vac. Sci. Technol. A **10**, 1389 (1992).

[6] M. Light and F. F. Chen, Phys. Plasmas **2**, 1084 (1995).

[7] M. Light, I. D. Sudit, F. F. Chen, and D. Arnush, Phys. Plasmas **2**, 4094 (1995).

[8] I. D. Sudit and F. F. Chen, Plasma Sources Sci. Technol. **5**, 43 (1996).

[9] A. W. Degeling, C. O. Jung, R. W. Boswell, and A. R. Ellingboe, "Effective ionization by helicon waves," submitted to Phys. Plasmas.

[10] I. D. Sudit and F. F. Chen, Plasma Sources Sci. Technol. **3**, 602 (1994).

[11] B. M. Harvey and C. N. Lashmore-Davies, Phys. Fluids B **5**, 3864 (1993).

[12] R. A. Helliwell, *Whistlers and Related Ionospheric Phenomena* (Stanford University Press, Stanford, CA, 1965).

[13] K. P. Shamrai and V. B. Taranov, Phys. Lett. A **204**, 139 (1995).

[14] F. F. Chen and C. D. Decker, Plasma Phys. Controlled Fusion **34**, 635 (1992).

[15] F. F. Chen, in *Physics of Laser Plasma*, edited by A. M. Rubenchik and S. Witkowski (Vol. 3, of *Handbook of Plasma Physics*, edited by M. N. Rosenbluth and R. Z. Sagdeev) (Elsevier Science Publishers B. V., Amsterdam, 1992), pp. 483–517.

[16] G. Chevalier and F. F. Chen, J. Vac. Sci. Technol. A **11**, 1165 (1993).

[17] P. K. Loewenhardt, B. D. Blackwell, and S. M. Hamberger, Plasma Phys. Controlled Fusion **37**, 229 (1995).

[18] R. J. Taylor, R. W. Conn, B. D. Fried, R. D. Lehmer, J. R. Liberati, P. A. Pribyl, L. Schmitz, G. R. Tynan, and B. C. Wells, in *Plasma Physics and Controlled Nuclear Fusion Research 1990* (International Atomic Energy Agency, Vienna, 1991), Vol. I, p. 463.

[19] T. Watari, T. Hatori, R. Kumazawa, S. Hidekuma, T. Aoki, T. Kawamoto, M. Inutake, S. Hiroe, A. Nishizawa, K. Adati, T. Sato, T. Watanabe, H. Obayashi, and K. Takayama, Phys. Fluids **21**, 2076 (1978).